Energy &
Environmental Science

RSCPublishing

PAPER

View Article Online
View Journal | View Issue

Precipitation in aqueous lithium–oxygen batteries: a model-based analysis

Cite this: *Energy Environ. Sci.*, 2013, **6**, 1299

Birger Horstmann,*[abc] Timo Danner[abc] and Wolfgang G. Bessler[abd]

Received 7th December 2012
Accepted 31st January 2013

DOI: 10.1039/c3ee24299d

www.rsc.org/ees

In this paper we present a model of the discharge of a lithium–oxygen battery with aqueous electrolyte. Lithium–oxygen batteries (Li–O_2) have recently received great attention due to their large theoretical specific energy. Advantages of the aqueous design include the stability of the electrolyte, the long experience with gas diffusion electrodes (GDEs), and the solubility of the reaction product lithium hydroxide. However, competitive specific energies can only be obtained if the product is allowed to precipitate. Here we present a dynamic one-dimensional model of a Li–O_2 battery including a GDE and precipitation of lithium hydroxide. The model is parameterized using experimental data from the literature. We demonstrate that GDEs remove power limitations due to slow oxygen transport in solutions and that lithium hydroxide tends to precipitate on the anode side. We discuss the system architecture to engineer where nucleation and growth predominantly occurs and to optimize for discharge capacity.

Broader context

Rechargeable batteries are generally believed to be an important ingredient in future carbon-neutral energy systems, both for stationary and mobile applications. Stationary applications primarily demand low cost per energy stored, while mobile ones demand low mass per energy stored. Because standard lithium intercalation batteries cannot meet all application requirements for, for example, electric vehicles and grid storage, new battery concepts are currently explored relying on conversion chemistries. During operation of conversion batteries, crystalline phases are formed inside the battery cell. Especially lithium–oxygen batteries receive great attention due to their potentially large gravimetric energy density. In lithium–oxygen batteries, lithium ions and oxygen molecules react to form solid reaction products. Most research is focused on batteries with organic electrolytes where lithium peroxide is formed. Here we provide a model-based analysis of lithium–oxygen batteries with aqueous electrolyte and highlight their advantages. Interestingly, the reaction product first dissolves in the electrolyte before it precipitates as solid lithium hydroxide monohydrate. Our model predicts that precipitation occurs outside the electrode explaining earlier experimental observations. This is advantageous as the electronically insulating precipitates do not hinder the electrode reactions as observed for organic electrolytes.

1 Introduction

The lithium–oxygen (Li–O_2) chemical system is a promising candidate for next-generation batteries. Above all, their theoretical energy density is outstanding.[1–6] In this respect, several designs with various electrolytes have been proposed. Most experiments and models focus on liquid aprotic electrolytes, but the ones used in state-of-the-art lithium-ion batteries decompose in the positive electrode during cycling.[7–14] Solid electrolytes grant stability, but their ionic conductivities are low at room temperature.[15,16] In this paper we illustrate that designs based on aqueous electrolytes are viable alternatives:[17–22]

(1) Oxygen reduction and evolution are well studied and reversible (*cf.*, alkaline fuel cells and electrolyzers[23]).

(2) Aqueous electrolytes offer a large ionic conductivity, not requiring thin-film electrodes (*cf.*, Pb battery[17]).

(3) Water is highly abundant and environmentally friendly.

Some challenges with Li–O_2 batteries remain:

(1) Oxygen solubility and diffusivity are low.[24]

(2) The reaction product lithium hydroxide precipitates and blocks transport paths.[25]

(3) The lithium metal anode strongly reacts with water.

(4) In contact with carbon dioxide lithium carbonates are formed.[26]

In the present work, we circumvent the last two challenges with adjusted model assumptions. Our model assumes the availability of a perfect lithium conducting membrane. Lithium ions can pass this infinitely thin layer without any resistance; all other species cannot pass it. We further assume to work with pure oxygen instead of ambient air. In this way, we can model fully functioning cells.

In this article, we address the first two challenges, that is, oxygen transport and precipitation, and show that these do not represent major obstacles in aqueous-electrolyte based Li–O_2 cells. In aqueous electrolytes, gas diffusion electrodes (GDE) are

---

[a] *German Aerospace Center (DLR), Institute of Technical Thermodynamics, Pfaffenwaldring 38–40, 70569 Stuttgart, Germany. E-mail: birger.horstmann@dlr.de*

[b] *Stuttgart University, Institute of Thermodynamics and Thermal Engineering (ITW), Pfaffenwaldring 6, 70569 Stuttgart, Germany*

[c] *Helmholtz Institute Ulm (HIU) Electrochemical Energy Storage, Albert-Einstein-Allee 11, 89081 Ulm, Germany*

[d] *Offenburg University of Applied Sciences, Badstraße 24, 77652 Offenburg, Germany*

frequently used, for example, for sensors and fuel cells.[27] In GDEs hydrophobic material, *e.g.*, polytetrafluoroethylene (PTFE) or polyvinylidene fluoride (PVDF), enables the coexistence of gaseous and aqueous phases. If oxygen is supplied to the reaction centers through the gas phase of such GDEs, oxygen transport does not limit the cell performance. In this study, we compare the performance of cells with flooded electrodes to ones with GDEs.

During discharge of an aqueous Li–O_2 battery, lithium ions are produced in the anode and hydroxide ions in the cathode until the dissolved LiOH concentration reaches its solubility limit $c_s \approx 5.2$ mol l^{-1} (T = 298.15 K). When discharge continues, lithium hydroxide monohydrate ($LiOH \cdot H_2O$) precipitates. The theoretical energy density of this battery with respect to the mass of water when discharged from $c_{OH^-} = 0$ to $c_{OH^-} = c_s$ is

$$E = \frac{Fc^{s}_{LiOH}U_0}{\rho_{H_2O}} = 490\ \mathrm{W\ h\ kg^{-1}}, \tag{1}$$

whereas the theoretical energy density of a cell fully discharged to solid $LiOH \cdot H_2O$ is

$$E = \frac{FU_0}{M_{LiOH \cdot H_2O}} = 2200\ \mathrm{W\ h\ kg^{-1}}. \tag{2}$$

Thus, the solid form of the final reaction product is indispensable to reach the energy density of current lithium intercalation technologies.[2] However, solid $LiOH \cdot H_2O$ can block transport paths.[28] Our simulations based on the classical theory of nucleation and growth show that $LiOH \cdot H_2O$ particles predominantly nucleate close to the lithium anode, that is, not in the cathode, in agreement with experimental findings.[20] This results from a salt concentration gradient in the cell. We will discuss how cells could be designed to influence precipitation and avoid pore blocking.

Modeling batteries aims at understanding experimental results and evaluating potential cell concepts. Continuum simulations at the cell level were pioneered by Newman,[29] who coupled the ionic transport in porous electrodes with Butler–Volmer kinetics at the active surfaces.[30] Recently, phase transformation kinetics in batteries became an important topic.[31] Major electrode materials, *e.g.*, lithium iron phosphate, undergo phase transformations during battery operation that result in distinct features in cell voltage. Models of such batteries combine transport in porous media with phase transformation kinetics in active particles. On the one hand, inhomogeneities in the reaction rates emerge even on the micro-scale and electrolyte transport is crucial.[30,32–37] On the other hand, the description of phase boundaries inside active particles requires a thermodynamically consistent approach that allows us to include the full variational chemical potential.[38] Under certain conditions this results in suppression of phase separation.[32,39–41] Next-generation battery chemistries such as lithium–air or lithium–sulfur represent a different class of phase-change systems, where phases do not transform inside solid particles or only on active surfaces, but also in the bulk electrolyte.

Despite considerable experimental activities on Li–O_2 batteries, only few modeling studies have been shown so far. Most modeling activities treat Li–O_2 batteries with aprotic electrolytes,[42–47] and focus on the deposition of solid lithium oxides or lithium carbonates in the cathode. On the one hand, these deposits can block pore space and inhibit the transport of oxygen into the cathode.[42–44,46,47] Since most oxygen is available at the oxygen inlet, reaction products tend to deposit there, so that finally oxygen cannot enter the cathode. On the other hand, these isolating deposits can passivate active surfaces.[45] To the best of our knowledge, only one single model for aqueous electrolytes has been published.[28] This model treats the oxygen reduction reaction and the subsequent precipitation of lithium hydroxide monohydrate within a single global reaction in a flooded cathode. Therefore, it predicts that $LiOH \cdot H_2O$ crystallizes in the cathode and blocks pore space. Our model, instead, takes into account the specifics of aqueous electrolytes and presents approaches to influence precipitation.

This paper contains a comprehensive model of the cell due to the lack of data on experimental Li–O_2 batteries with aqueous electrolytes. Our basic principle for model development is to make the simplest realistic assumptions. At the present stage, the model allows us to predict why a cell fails, but not when it fails. Even though experimental validation is still missing, the model allows analyzing potential design and operation scenarios.

Our paper is structured as follows. We present the mathematical and physical description of our model in Section 2. We arrange this presentation into physical topics, that is, electrochemical reactions, oxygen dissolution, transport phenomena, phase coexistence in GDEs, and precipitation. In Section 3 we present the parameterization of the model based on the literature available for aqueous solutions. We find in Section 4.1 that preferential nucleation close to the anode can be the capacity-limiting process in Li–O_2 batteries. In Section 4.2 we address power limitations during battery discharge in flooded electrodes and in GDEs. We discuss in Section 4.3 implications of our findings on potential cell architecture. Finally, we conclude in Section 5.

2 Physical and mathematical model

In this section our model framework is outlined, which is partially relevant for a wider range of electrochemical systems, for example, the dynamic gas diffusion electrode or the precipitation, as occurring in fuel cells and non-aqueous Li–O_2 batteries. We begin by outlining our implementation of classical electrochemical modeling,[30] *i.e.*, electrochemistry (see Section 2.2), oxygen dissolution (see Section 2.3), and convective transport (see Section 2.4). Then we discuss the phase coexistence of gaseous and liquid phases in gas diffusion electrodes (see Section 2.5). Finally, we extract the kinetics of crystallization from the classical theory of nucleation and growth in Section 2.6.

2.1 Computational domain

During discharge of a Li–O_2 battery, oxygen enters the GDE from a gas channel and dissolves in the aqueous electrolyte (see

Fig. 1). At catalytically active surfaces in the cathode, oxygen and water electrochemically react to form hydroxide ions. While these OH^- ions migrate through the cell to the anode, the Li^+ counter-ions migrate in the opposite direction. They are electrochemically formed at a lithium metal foil, pass a lithium-ion-conducting membrane, which prevents direct contact between lithium metal and the aqueous electrolyte, and dissolve in the electrolyte. Lithium hydroxide monohydrate particles will nucleate when the ion concentration increases sufficiently beyond its solubility limit. In the GDE, gaseous oxygen and liquid electrolyte coexist. On the one hand, an overpressure tries to push water into the GDE, on the other hand, the capillary effect of hydrophobic binders, *e.g.*, PTFE or PVDF, tries to keep it out and leave space for the gas phase.

We model these processes along a single direction, associated with the *y*-coordinate, and divide the computational domain into the lithium anode, the separator, the cathode, and the gas channel. The details of our model are outlined below as a combination of transport physics and chemical reactions. Even though our model is intrinsically dynamic, we make sure that it is thermodynamically consistent and describes stationary states correctly. All symbols are defined in the List of symbols.

2.2 Electrochemical reactions

Two electrochemical half-cell reactions enter our model. In the anode, lithium dissolves in the electrolyte

$$\mathrm{Li} \rightleftarrows \mathrm{Li}^+ + \mathrm{e}^-. \tag{3}$$

The reaction rate is calculated with global (*i.e.*, single-step) electrochemical kinetics

$$\dot{s}_{an} = k^f_{an}\exp\left(-\alpha_{an}\frac{F\Delta\Phi_{an}}{RT}\right) - k^r_{an}c_{Li^+}\exp\left((1-\alpha_{an})\frac{F\Delta\Phi_{an}}{RT}\right) \tag{4}$$

where $\Delta\Phi_{an} = \Phi_{an} - \Phi_{elyte}$ is the potential step between the lithium anode and the electrolyte. The cathodic oxygen reduction reaction in alkaline water

$$\mathrm{O}_2^{aq} + 2\,\mathrm{H_2O} + 4\,\mathrm{e}^- \rightleftarrows 4\,\mathrm{OH}^- \tag{5}$$

is also modeled by global kinetics

$$\dot{s}_{ca} = k^f_{ca}c_{O_2}c_{H_2O}{}^2\exp\left(-\alpha_{ca}\frac{F\Delta\Phi_{ca}}{RT}\right) - k^r_{ca}c_{OH^-}{}^4\exp\left((1-\alpha_{ca})\frac{F\Delta\Phi_{ca}}{RT}\right). \tag{6}$$

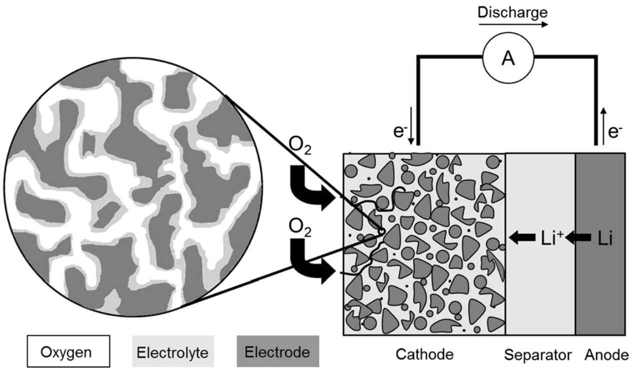

Fig. 1 Schematic representation of a Li–O_2 battery with a gas diffusion electrode.

Thermodynamics determines the open-circuit voltage under equilibrium conditions ($\dot{s}_{ca} = \dot{s}_{an} = 0$). Consequently, the rates of the reverse reactions k^r_{an}, k^r_{ca} are calculated from the rates of the forward reaction, $k^r_{an} = k^f_{an}c_{Li^+}{}^{-1}\exp(\Delta\mu_{an}/RT)$ and $k^r_{ca} = k^f_{ca}c_{O_2}c_{H_2O}{}^2c_{OH^-}{}^{-4}\exp(\Delta\mu_{ca}/RT)$, where $\Delta\mu_{an}$ and $\Delta\mu_{ca}$ are the Gibbs reaction enthalpies.[48]

2.3 Oxygen dissolution

Dissolution from gaseous phases is thermodynamically described by Henry's law, $c^s_{O_2} = Hp_{O_2}$ with the solubility $c^s_{O_2}$. Henry's law does not include kinetics. Therefore, we model oxygen dissolution within our framework as chemical reaction (see ref. 47)

$$\mathrm{O}_2^{g} \leftrightarrows \mathrm{O}_2^{aq}. \tag{7}$$

Thus, we can naturally model the oxygen dissolution kinetics with the rate equation

$$\dot{s}_s = k^f_s p_{O_2} - k^r_s c_{O_2} \tag{8}$$

The solubility is determined by the equation $\dot{s}_s = 0$, *i.e.*, by the ratio of the reaction rates. We choose to parameterize the solubility *via* thermodynamic data and set

$$\frac{k^r_s}{k^f_s} = \frac{p_{O_2}}{c_{O_2}}\exp\left(\frac{\Delta\mu_s}{RT}\right). \tag{9}$$

We determine the forward rate constant $k^f_s = 0.01(2\pi M_{O_2}RT)^{-0.5}$ from the Hertz–Knudsen equation,[49] assuming that one percent of gas particles hitting the phase boundary enter the liquid.

2.4 Transport

Three transport mechanisms are relevant in this article: diffusion and migration of dissolved species, convection of the liquid solvent, and convection of the gas phase.

Lithium and hydroxide ions as well as oxygen molecules are dissolved in the electrolyte. While oxygen travels from the gas channel to the cathode surface, the lithium hydroxide ions carry charge between the electrodes. First, we describe the transport of this binary salt with concentrated solution theory.[29,50] We reformulate the traditional equations.[47] The concentrations of dissolved particles obey the continuity equations

$$\frac{\partial(\varepsilon_{elyte}c_i)}{\partial t} = -\mathrm{div}\vec{j}^{\,D}_i - \mathrm{div}\vec{j}^{\,M}_i - \mathrm{div}\left(c_i\vec{v}_{elyte}\right) + A^{spez}\dot{s}_i. \tag{10}$$

The third term in eqn (10) is due to the convective transport of the electrolyte (see eqn (15)), the fourth term is the total production rate due to reactions (see Sections 2.1, 2.2, and 2.5),[47] and the first two terms are the ionic currents due to diffusion and migration, respectively. For lithium c_+ and hydroxide c_- ions the latter are determined by

$$\vec{j}^{\,\mathrm{D}}_{\pm} = -\varepsilon^{\beta}_{\mathrm{elyte}} D_{\pm} \mathrm{grad} c_{\pm}, \vec{j}^{\,\mathrm{M}}_{\pm} = -\varepsilon^{\beta}_{\mathrm{elyte}} D^{\mathrm{M}}_{\pm} \mathrm{grad} \Phi_{\mathrm{elyte}}. \tag{11}$$

The diffusion and migration coefficients are chosen according to concentrated solution theory

$$D_{\pm} = D_0 + \frac{t_{\pm}}{z_{\pm}F}\frac{\kappa^{\mathrm{D}}}{c_{\pm}} \quad \text{and} \quad D^{\mathrm{M}}_{\pm} = \frac{t_{\pm}}{z_{\pm}F}\kappa \tag{12}$$

with $\kappa^{\mathrm{D}} = 2/z_+F(t_+ - 1)c_+\kappa\partial\mu_+/\partial c_+$. Here t_+ is the transference number of lithium ions, D_0 is the self-diffusion coefficient of lithium hydroxide salt, and κ is its conductivity. The Bruggeman coefficient β takes into account the porosity and tortuosity of the medium. We achieve electro-neutrality by postulating local charge conservation

$$\begin{aligned} 0 &= \sum_i z_i F \frac{\partial\left(\varepsilon_{\mathrm{elyte}} c_i\right)}{\partial t} \\ &= \sum_i z_i F \left[-\mathrm{div}\vec{j}^{\,\mathrm{D}}_i - \mathrm{div}\vec{j}^{\,\mathrm{M}}_i - \mathrm{div}\left(\varepsilon_{\mathrm{elyte}} c_i \vec{v}_{\mathrm{elyte}}\right) + A^{\mathrm{spez}} \dot{s}_{\mathrm{i}} \right] \end{aligned} \tag{13}$$

and choosing electro-neutral initial conditions. Eqn (13) determines the electric potential Φ_{elyte}. We assume here that the transport of dissolved oxygen molecules does not influence the ionic transport.[44,45] In the case of neutral oxygen molecules, the fluxes in eqn (10) are given by

$$\vec{j}^{\,\mathrm{D}}_{\mathrm{O_2}} = -\varepsilon^{\beta}_{\mathrm{elyte}} D_{\mathrm{O_2}} \mathrm{grad} c_{\mathrm{O_2}} \quad \text{and} \quad \vec{j}^{\,\mathrm{M}}_{\mathrm{O_2}} = 0. \tag{14}$$

Eqn (11)–(14) describe the transport of all dissolved species relative to the solvent. The dynamics of the solvent, however, are treated differently. In a closed battery cell, solvent transport is a minor effect and disregarded in typical models.[30] In an open Li–O_2 battery with a GDE, solvent transport is a major issue for two reasons. Firstly, the solvent H_2O is consumed in the cathode during discharge making a constant flux of water into the GDE necessary. Secondly, the phase coexistence of gas and liquid in the GDE requires knowledge of the state of each phase, including pressure (see Section 2.4). A pressure gradient drives water transport and in turn water transport reduces the pressure gradient.

We determine the solvent velocity from Darcy's law, inspired by fuel cell models,[51]

$$\vec{v}_{\mathrm{elyte}} = -\frac{B_{\mathrm{elyte}}}{\eta_{\mathrm{elyte}}} \mathrm{grad} p_{\mathrm{elyte}} \tag{15}$$

with the viscosity η_{elyte} of the liquid phase. The oxygen gas obeys the analogous equation[48]

$$\vec{v}_{\mathrm{gas}} = -\frac{B_{\mathrm{gas}}}{\eta_{\mathrm{gas}}} \mathrm{grad} p_{\mathrm{gas}}, \tag{16}$$

where η_{gas} is the viscosity of gaseous oxygen.

2.5 Gas diffusion electrode

Gas diffusion electrodes (GDEs) contain hydrophobic materials, *e.g.*, PTFE or PVDF. Therefore, the aqueous electrolyte cannot fully flood the electrode. The coexistence of liquid electrolyte and gaseous oxygen in a GDE for a Li–O_2 battery allows for significantly faster oxygen flow towards the electro-active sites *via* the gas phase (see Fig. 1).

As shown below, our description of multi-phase transport in GDEs takes into account the real equation of state of the liquid phase, rarely done in battery modeling. This is crucial here in order to simulate the consumption of solvent at nearly constant salt concentration.

We keep track of the states of the coexisting phases through macroscopic parameters along the computational direction, for example, $\varepsilon_s(y)$, $p_s(y)$, and balance their pressures with an empirical coarse-grained approach.[52–54] In this way, we neglect details of the complex pore network containing hydrophilic/hydrophobic and microscopic/mesoscopic pores. More sophisticated approaches are employed in some steady-state fuel cell models,[27] which are, however, beyond the scope of the present modeling approach.

In the following, we outline our model equations. Phase coexistence is constrained by the total volume at each position y

$$\sum_s \varepsilon_s(p_s) = 1, \tag{17}$$

where the sum extends over all phases s. The volume fractions ε_s depend on the pressures p_s of the phases. In a Li–O_2 battery under regular operating conditions, only liquid and gas are compressible and depend on pressures. Therefore, eqn (17) represents a condition for the pressures of the gas phase p_{gas} and the liquid phase p_{elyte}. In the hydrophobic environment of the GDE, the aqueous phase has a larger pressure than the gaseous phase. This phenomenon is analogous to regular capillary depression. We describe it with the empirical law[52–54]

$$p_{\mathrm{capillary}} = p_{\mathrm{gas}} - p_{\mathrm{elyte}} = -J(s), \tag{18}$$

where $J(s)$ is the Leverett function and $s = \varepsilon_{\mathrm{elyte}}(\varepsilon_{\mathrm{elyte}} + \varepsilon_{\mathrm{gas}})^{-1}$ is the saturation of the liquid phase in the free pore space. The equation of state $\varepsilon_{\mathrm{gas}}(p_{\mathrm{gas}})$ is given by the ideal gas law

$$p_{\mathrm{gas}} V_{\mathrm{gas}} = N_{\mathrm{gas}} RT \tag{19}$$

and the equation of state $\varepsilon_{\mathrm{elyte}}(p_{\mathrm{elyte}})$ by[67]

$$\sum_i \frac{\partial V_{\mathrm{elyte}}}{\partial N_i} c_i = \varepsilon_{\mathrm{elyte}}. \tag{20}$$

Eqn (20) follows from basic thermodynamics valid for any phase. The partial molar volume $\partial V_{\mathrm{elyte}}/\partial N_i$ of species i splits up into two parameters, the partial molar volume $\bar{V}$ at standard pressure p_0 and the partial molar compressibility $\bar{\kappa}$

$$\frac{\partial V_{\mathrm{elyte}}}{\partial N_i} = \bar{V}_i + (p - p_0)\bar{\kappa}_i \tag{21}$$

With these equations of state at hand, we can determine the pressures p_{gas} and p_{elyte} based on eqn (17) and (18). Since the gas phase is absent outside the GDE, eqn (17) (together with eqn (20)) suffices to determine the system dynamics there.

2.6 Nucleation and growth

Because precipitation of lithium hydroxide monohydrate $\mathrm{LiOH{\cdot}H_2O}$

$$\mathrm{Li}^{+(\mathrm{aq})} + \mathrm{OH}^{-(\mathrm{aq})} + \mathrm{H_2O} \rightleftarrows \mathrm{LiOH{\cdot}H_2O} \qquad (22)$$

determines the discharge capacity of an aqueous Li–O$_2$ battery (see Section 4), we develop a detailed model of its kinetics. When the salt concentration $c_{\mathrm{Li}^+} = c_{\mathrm{OH}^-}$ increases sufficiently beyond the solubility limit $c^{\mathrm{s}}_{\mathrm{Li}^+}$, small stable crystal clusters nucleate and start to grow. The process of precipitation involves two main steps, nucleation of seed crystals and subsequent growth of nuclei. It is governed by the quantum behavior of crystals containing ~10 particles and the classical behavior of crystals of size ~1 mm. Consequently, mechanisms of precipitation strongly vary with precipitate and conditions. We choose to model precipitation within the classical theory of nucleation and growth (CNG).[55–58] The theoretical validity of this phenomenological theory has been a subject of discussions,[55] but it has been shown to agree with experiments after adjusting its parameters.[59] In Section 4.3 we analyse the sensitivity of our model to the critical parameters. The CNG assumes that the reaction enthalpy of formation of a single crystal nucleus of size n consists of a bulk and a surface term[55–58]

$$\Delta G = \Delta G_{\mathrm{V}} + \Delta G_{\mathrm{A}} = -n2kT\ln S + A(n)\gamma, \qquad (23)$$

where γ is the macroscopic surface energy and the factor of 2 arises for a binary salt. The supersaturation ratio $S = c_{\mathrm{Li}^+}/c^{\mathrm{s}}_{\mathrm{Li}^+}$ is the driving force for nucleation. For larger nucleus sizes the bulk energy is increasingly negative, whereas the surface energy is increasingly positive. Thus, the former dominates for large crystals and the latter for small crystals. In Fig. 2 we illustrate that the nucleus formation energy ΔG passes a maximum at a critical nucleus size n_{crit}. Crystal clusters must exceed this critical size before they can grow in a stable way. In the case of heterogeneous disc-shaped nucleation[58] the critical formation energy is

$$\Delta G_{\mathrm{crit}} = \frac{\gamma^2 a^4}{2kT\ln S}. \qquad (24)$$

The rate of nucleation of critical nuclei is then estimated as[55]

$$\dot{N} = D_0 a_{\mathrm{D}}{}^{-2} Z N_0 \exp\left(-\frac{\Delta G_{\mathrm{crit}}}{kT}\right). \qquad (25)$$

Here the last term represents the activation of a critical complex from thermal fluctuations, N_0 is the number of sites on which nucleation can occur, the Zeldovich factor $Z = (\Delta G_{\mathrm{crit}}/3\pi kT)^{0.5}/n_{\mathrm{crit}}$ expresses the fact that a critical nucleus can disintegrate again, and the activation frequency for diffusion $D_0 a_{\mathrm{D}}{}^{-2}$ describes a diffusion-limited nucleation process. It is difficult to determine N_0, we will address this issue below.

After this brief discussion of nucleation, we turn to crystal growth. In the simplest case, one can assume linear growth. This is predicted by the excellent bulk diffusion model[55] at large supersaturation ratios $S > 10^{-5}$, which we generally find in our case. Furthermore, linear growth is observed experimentally for quite soluble substances like, for example, potassium chloride.[60,61] The reaction rate for this growth process is

$$\dot{s}_{\mathrm{cryst}} = \frac{D_0}{\delta}\left(c_{\mathrm{Li}^+} - c^{\mathrm{s}}_{\mathrm{Li}^+}\right), \qquad (26)$$

where δ is the diffusion layer thickness. We treat the diffusion layer thickness as a parameter (see below).

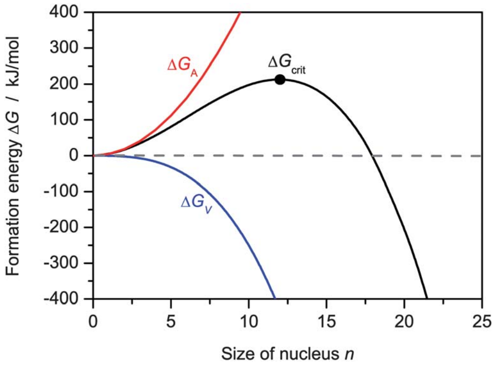

Fig. 2 Formation energy of crystal nucleus consisting of n particles. The bulk contribution ΔG_{V} is decreasing with size and the surface contribution ΔG_{A} is increasing with size. The total formation energy goes through a maximum at the critical energy ΔG_{crit}.

After summarizing the results of CNG in eqn (25) and (26), we are now describing the application of this theory in the Li–O$_2$ battery model. In this paper we will distinguish two cases, firstly, nucleation on functional surfaces in the cathode and the separator (see Fig. 3a), and, secondly, nucleation on sedimenting dust particles in a separator of pure electrolyte (see Fig. 3b). These two models differ in the number of nucleation sites N_0 entering eqn (25) and, consecutively, in the specific area for crystal growth $A^{\mathrm{spez}}_{\mathrm{cryst}}$.

In the presence of surfaces as in the pore space of a GDE, heterogeneous nucleation on the surfaces (supports) usually dominates homogeneous nucleation. Exact modeling of heterogeneous nucleation requires knowledge of contact angles between crystalline and supporting materials. Battery cells,

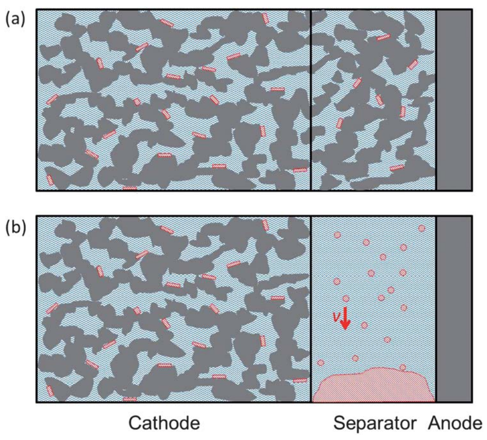

Fig. 3 Schematic depiction of precipitation kinetics: (a) nucleation on surfaces in a porous separator and a cathode, and (b) nucleation on dust particles inside a separating bulk electrolyte with sedimentation due to gravity.

however, contain plenty of different materials and surface morphologies so that an exact approach is not feasible. Thus, we assume disc-shaped heterogeneous nucleation valid for nucleation on crystal material itself (see Fig. 3a). The area supporting the nucleus evolves according to

$$\frac{\partial A^{\mathrm{spez}}_{\mathrm{cryst}}}{\partial t} = \pi r_{\mathrm{crit}}{}^{2}\dot{N}(N_0) \quad \text{with} \quad N_0 = A^{\mathrm{spez},0}_{\mathrm{cryst}} a^{-2}. \tag{27}$$

Here $A^{\mathrm{spez},0}_{\mathrm{cryst}}$ is the specific surface area of the pristine cathode/separator surfaces. $\mathrm{LiOH\cdot H_2O}$ can subsequently crystallize on top of these discs according to eqn (26), where we assume a constant diffusion layer thickness $\delta = \delta_0$ determined by the pore structure. Crystal growth is described with a single volume fraction

$$\frac{\partial \varepsilon_{\mathrm{cryst}}}{\partial t} = \dot{s}_{\mathrm{cryst}} A^{\mathrm{spez}}_{\mathrm{cryst}} V^{\mathrm{M}}_{\mathrm{cryst}}. \tag{28}$$

As a result, we simulate nucleation and growth of column-shaped crystals on surfaces in the cell.

In state-of-the-art lithium batteries, both the cathode and the separator are porous so that nucleation on surfaces will dominate. In the following we discuss an alternative cell design (see Fig. 3b). Due to the large ionic conductivity of aqueous electrolytes, *e.g.*, lead-acid batteries, a reservoir of pure electrolyte can serve as the separator, as proposed by Stevens *et al.*[20] In such separators, nucleation predominantly occurs on dust particles. These could be small amounts of foreign particles that enter the cell during its assembly, detached carbon particles, or $\mathrm{LiOH\cdot H_2O}$ particles from previous battery cycles. In fact, true homogeneous nucleation has been seldom measured. The crystal nuclei sediment due to gravity and form a reservoir of precipitates at the bottom of the cell. Under these conditions, crystal nuclei of different sizes coexist.[62] We evolve the size distribution of spherical crystal nuclei

$$N(r) = f(r)\mathrm{d}r \tag{29}$$

with radii r *via* the equation

$$\frac{\partial f(r)}{\partial t} = \dot{N}\mathrm{d}r_0{}^{-1}\delta_{r_0} - f\tau^{-1} - \frac{\partial}{\partial r}\left(f\frac{\mathrm{d}r}{\mathrm{d}t}\right). \tag{30}$$

The first term in eqn (30) describes nucleation of crystals, where the nucleation rate is $\dot{N}$ with a constant N_0 (see eqn (25)) and the first discretization compartment contains radii from 0 to $\mathrm{d}r_0$. The second term in eqn (30) describes sedimentation due to gravity, modeled as a decay process with typical time

$$\tau(r) = \frac{h\varepsilon_{\mathrm{elyte}}}{v(r)}. \tag{31}$$

Here h is the height of the battery and

$$v(r) = \frac{2}{9}r^2\frac{g\left(\rho_{\mathrm{LiOH\cdot H_2O}} - \rho_{\mathrm{elyte}}\right)}{\eta} \tag{32}$$

the sedimentation velocity from Stoke's law. The last term in eqn (30) represents crystal growth with radial growth rate[60]

$$\frac{\mathrm{d}r}{\mathrm{d}t} = V^{\mathrm{M}}_{\mathrm{cryst}}\dot{s}_{\mathrm{cryst}}(\delta), \tag{33}$$

where the diffusion layer thickness $\delta = r(1 + vr/D_0)^{-0.285}$ is determined by sedimentation.[56] By integrating the crystal size distribution we get the volume fraction $\varepsilon_{\mathrm{cryst}} = V^{\mathrm{M}}_{\mathrm{cryst}}N_{\mathrm{A}}{}^{-1}\int(4/3)\pi r^3 f\mathrm{d}r$ of sedimenting crystals and the volume fraction of the crystal reservoir at the cell bottom

$$\frac{\partial \varepsilon_{\mathrm{res}}}{\partial t} = V^{\mathrm{M}}_{\mathrm{cryst}}N_{\mathrm{A}}{}^{-1}\int\frac{4}{3}\pi r^3 f\tau^{-1}\mathrm{d}r + \dot{s}_{\mathrm{cryst}}A^{\mathrm{spez}}_{\mathrm{res}}V^{\mathrm{M}}_{\mathrm{cryst}}. \tag{34}$$

The second term in eqn (34) denotes direct crystal growth of the reservoir from solution if a film of $\mathrm{LiOH\cdot H_2O}$ had already been formed at the cell bottom, *i.e.*, $A^{\mathrm{spez}}_{\mathrm{res}} = h^{-1}$ for $\varepsilon_{\mathrm{res}} \geq r_{\mathrm{crit}}/h$ and $A^{\mathrm{spez}}_{\mathrm{res}} = 0$ for $\varepsilon_{\mathrm{res}} < r_{\mathrm{crit}}/h$. This is the same as heterogenous crystal growth (see eqn (28)).

The latter cell design with nucleation on dust particles contains a separator that can accommodate the precipitate. At the end of discharge, the separator should be completely and homogeneously filled with $\mathrm{LiOH\cdot H_2O}$ to increase capacity. This can be achieved, for example, by shaking the cell or stirring the crystal reservoir. We model stirring *via* a diffusion equation

$$\frac{\partial \varepsilon_{\mathrm{res}}}{\partial t} = -C\mathrm{div}(-\mathrm{grad}\varepsilon_{\mathrm{res}}). \tag{35}$$

that makes the reservoir homogeneous along the computational direction y.

3 Parameterization and computational details

In Section 2 we presented the general modeling approach. In this section we discuss the parameters for the specific simulation of an aqueous Li–O_2 battery. These parameters are based on measurements of lithium hydroxide solutions published in the literature. Our simulations are isothermal at temperature $T_0 = 298.15\ K$. However, we parameterize over a wide temperature range to support future studies on aqueous lithium batteries.

3.1 Geometric structure

We divide the computational domain into the oxygen channel, the cathode, and the separator (see Table 1). A lithium foil terminates the separator. We compare the performance of different cell designs. Thus, we distinguish between a standard cathode (a GDE, *cf.* Fig. 1), and an alternative cathode (a fully flooded cathode). We further distinguish between a standard separator (a porous one with surface nucleation, *cf.* Fig. 3a), and an alternative separator (containing only electrolyte with nucleation on sedimenting dust particles, *cf.* Fig. 3b). Gaseous oxygen can enter the cell from the channel; apart from this, the battery cell is closed.

In this paper, capacities are given with respect to the mass of water. The initial mass of water with respect to the cell area is 0.27 kg m^{-2} (GDE, surface nucleation), 0.29 kg m^{-2} (GDE, nucleation on dust particles), and 0.45 kg m^{-2} (flooded electrode, surface nucleation); the mass of carbon is 0.28 kg m^{-2} ($\rho_{\mathrm{S}} = 2260$ kg m^{-3}); the separator mass is negligible. The mass

Table 1 Structure of porous cell components. If two values are given in the cathode, the first corresponds to a cell with a GDE and the second to a cell with a flooded electrode. In the separator, the first corresponds to a cell with a porous separator and the second to a cell with a bulk separator region

Channel	**Pressure**	101 325 Pa
	Phases (species)	**Volume fraction**
	Gas (O_2^g)	1.0
Cathode	**Thickness**	500 μm
	Phases (species)	**Initial volume fraction**
	Gas (O_2)	0.375/0.0
	Liquid electrolyte (H_2O, Li^+, OH^-, O_2^{aq})	0.375/0.75
	$LiOH \cdot H_2O$	$0.0(\rho = 1510$ kg m$^{-3})$
	Carbon	0.25
Separator/anode	**Thickness**	100 μm
	Phases (species)	**Initial volume fraction**
	Liquid electrolyte (H_2O, Li^+, OH^-, O_2^{aq})	0.8/1.0
	$LiOH \cdot H_2O$	0.0
	Glass separator	0.2/0.0
	Lithium metal (Li^+)	0.0

of oxygen bound in the cell after discharge, 0.3 mg mA^{-1} h^{-1}, depends on capacity.

The height of the battery is $h = 10$ cm (entering the model in the case of sedimentation, see eqn (31)). The typical diffusion layer thickness in the GDE is $\delta_0 = 10$ μm (see eqn (26)). The balance between the volume fractions of gaseous oxygen and liquid electrolyte in GDEs is determined by capillary pressure (see eqn (18)). We describe it based on Kumbur *et al.*[52] with the Leverett function

$$J(s) = 1.5 \times 10^6[-0.000178T + 0.1247]\left(\frac{293\ \mathrm{K}}{T}\right)^6$$
$$[0.05(0.0469 - 0.00152 \cdot 0.05 - 0.0406s^2 + 0.1430s^3) + 0.0561\ln(s)] \quad (36)$$

for $s > 0.03$ and $J(s) = 0$ for $s \leq 0.03$. Eqn (36) describes a gas diffusion layer from SGL with five weight percent PTFE loading. We assume an ideal microporous layer that prevents the electrolyte from leaking into the oxygen channel. The stirring coefficient is $C = 10^{-9}$ m^2 s^{-1} (see eqn (35)).

3.2 Thermodynamics

The chemical potentials of species in the electrolyte are a function of the standard potentials μ_i^0, the activities a_i, the partial molar volumes $\bar{V}_i$, and the partial molar compressibilities $\bar{\kappa}_i$

$$\mu_i = \mu_i^0 + \ln a_i + \bar{V}_i(p - p_0) + \bar{\kappa}_i(p - p_0)^2. \quad (37)$$

The standard molar enthalpies h_i^Θ, entropies s_i^Θ, and capacities $c_i^{p,\Theta}$ for the species O_2^g, H_2O, Li^+, and OH^- are taken from Atkins' Physical chemistry.[63] From these values we calculate the temperature-dependent thermodynamic data for the standard states according to

$$H_i^0 = h_i^\Theta + (T - T^0)c_i^{p,\Theta}, \quad (38)$$

$$S_i^0 = s_i^\Theta + Rc_i^{p,\Theta}\ln(T/T^0) \quad (39)$$

$$\mu_i^0 = H_i^0 - TS_i^0. \quad (40)$$

The remaining thermodynamic parameters are found in the context of LiOH and O_2^{aq} solubilities below.

The solubility of oxygen in alkaline water strongly depends on the salt concentration, an effect referred to as salting-out. If lithium hydroxide is added to the solution, the solubility of oxygen is reduced and gaseous molecular oxygen evolves. First, we parameterize the solubility in pure water with the measurements reviewed by Tromans.[64] We deduce as standard thermodynamic properties $h_{O_2}^\Theta = 5.090$ kJ mol^{-1}, $s_{O_2}^\Theta = 166.95$ J mol^{-1} K^{-1}, and $c_{O_2}^{p,\Theta} = 209.35$ J mol^{-1} K^{-1} in the concentration scale. Salting-out is described *via* the empirical Setchenov relation[65]

$$\left(\mu_{O_2} - \mu_{O_2}^0\right)\Big/RT = \ln\left(\frac{c_{O_2}}{\mathrm{mol\ l^{-1}}}\right) + k_{\mathrm{sca}}c_{\mathrm{Li}^+}. \quad (41)$$

From the measurements of Lang and Zander[65] and Elliot *et al.*[66] we deduce $k_{\mathrm{sca}} = 0.01057/(T - 277)$. In Fig. 5 we show that the solubilities obtained in this way agree well with the measurements of Elliot *et al.*,[66] but disagree with the measurements of Lang and Zander[65] However, the trend of the latter agrees with our fit (see Fig. 5).

Measurements of the solubility of lithium hydroxide in water are reviewed in the work of Monnin and Dubois.[25] In this reference, the activities of the solution are taken into account. These are fitted with the Pitzer formalism in the molality scale, which is based on the Debye–Hückel theory.[67] The correct fit for the Pitzer parameter A^Φ is given in ref. 68. The thermodynamic data of $LiOH \cdot H_2O$ are $h_{LiOH \cdot H_2O}^\Theta = -787.07$ kJ mol^{-1}, $s_{LiOH \cdot H_2O}^\Theta = 83.352$ J^{-1} mol^{-1} K^{-1}, and $c_{LiOH \cdot H_2O}^{p,\Theta} = 9.7674$ J mol^{-1} K^{-1}, as determined from the solubility data reviewed in the work of Monnin and Dubois (see Fig. 4).[25]

We further determine the partial molar volumes of H_2O, Li^+, and OH^- from the measurements of Herrington *et al.*[69] and

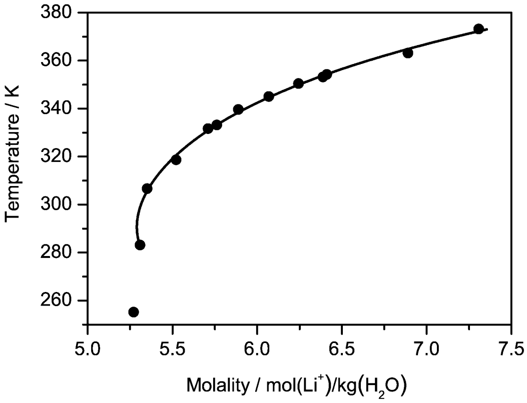

Fig. 4 Solubility of lithium hydroxide in aqueous solution for various temperatures. The symbols represent measurements by Monnin and Dubois[25] The solid line represents the fit with thermodynamic data $h_{LiOH \cdot H_2O}^\Theta$, $s_{LiOH \cdot H_2O}^\Theta$, and $c_{LiOH \cdot H_2O}^{p,\Theta}$ (see text).

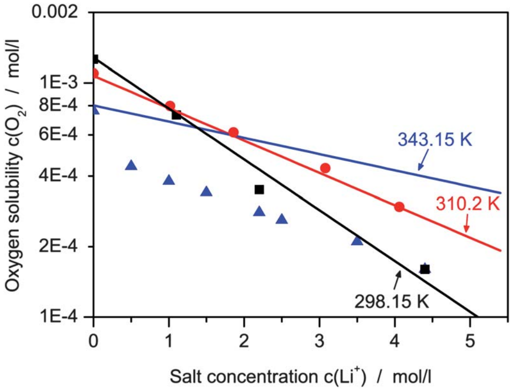

Fig. 5 Oxygen solubility at various salt concentrations and temperatures. The black squares and red circles represent measurements by Elliot *et al.*,[66] the blue triangles represent measurements by Lang and Zander.[65] The solid lines represent fits according to eqn (41).

Roux *et al.*[70] In Fig. 6 we compare our fit with these measurements, which are scarce at high salt concentrations. The partial molar volumes $\bar{V}_i$ are fitted with the Pitzer formalism again (this is possible because $\bar{V}_i = \partial\mu_i/\partial p$ holds), where we include the volumes at infinite dilution as additional parameters.[67,69] The Pitzer parameters are given in Table 2.

We parameterize the partial molar compressibilities according to Millero *et al.*[71] for NaOH, but exchange the partial molar compressibility of Li$^+$ at infinite dilution with the measurement of Roux *et al.*[70] for LiOH. The partial volumes and compressibilities are important for the liquid equation of state only (see eqn (20) and (21)). Thus, we neglect the partial molar volume of dissolved oxygen due to its low concentration ($\bar{V}_{O_2} = \bar{\kappa}_{O_2} = 0$).

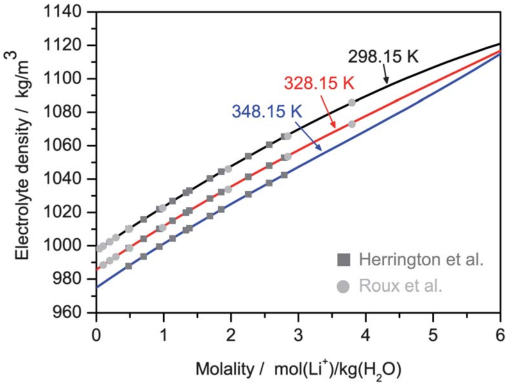

Fig. 6 Density of lithium hydroxide solution at various salt concentrations and temperatures. The squares and circles refer to the measurements of Herrington *et al.*[69] and Roux *et al.*[70] respectively.

3.3 Transport and kinetics

Electrolyte transport properties strongly depend on viscosity η. The viscosity of lithium hydroxide solutions was measured by Laliberte.[72] With the Einstein–Stokes relationship, we extend the range of measurements of lithium diffusivity at infinite dilution[73]

$$\begin{aligned} D_\pm = 6.8 \times 10^{-9}\ \ \mathrm{m}^2\ \mathrm{s}^{-1} \frac{\eta_{\mathrm{H_2O}}}{\eta} \frac{T}{T_0} \big[& 8.90466 \times 10^{-4} {m_{\mathrm{Li}^+}}^4 \\ & - 0.0127732 {m_{\mathrm{Li}^+}}^3 + 0.0538298 {m_{\mathrm{Li}^+}}^2 - 0.0381098 m_{\mathrm{Li}^+} \\ & + 0.856882 \big] \end{aligned} \tag{42}$$

and the oxygen diffusivity in pure water[74]

$$D_{\mathrm{O_2}} = 1.693 \times 10^{-6}\ \mathrm{m}^2\ \mathrm{s}^{-1} \frac{\eta_{\mathrm{H_2O}}}{\eta} \exp\left(-\frac{16\,739\ \ \mathrm{J\ mol}^{-1}}{RT} \right) \tag{43}$$

to a wider range of salt concentrations and temperatures. The conductivity of a lithium hydroxide solution is[75]

$$\begin{aligned} \kappa = (-37.72629 + 0.13245 T/\mathrm{K}) - (27.60862 \\ - 0.14199 T/\mathrm{K}) m_{\mathrm{Li}^+} - 1.39623 {m_{\mathrm{Li}^+}}^2 \end{aligned} \tag{44}$$

and the transference number is

$$t_+ = 0.1637 \tag{45}$$

We use the standard Bruggeman coefficient $\beta = 1.5$.[29] Convective transport is governed by the permeabilities (see eqn (15) and (16)),[76] in the GDE we use

$$B_{\mathrm{gas}} = 5 \times 10^{-12}\ \mathrm{m}^2 (1-s)^{3.5},\ B_{\mathrm{elyte}} = 5 \times 10^{-12}\ \mathrm{m}^2 \times s^{3.5}. \tag{46}$$

In the separator we employ the quasi-infinite permeability

$$B_{\mathrm{elyte}} = 10^{-9}\ \mathrm{m}^2.$$

The kinetics of the (electro-)chemical reactions depend on the specific surface areas and the forward reaction rates. In this paper, the former are $A_{\mathrm{ca}}^{\mathrm{spez}} = 10^6\ \mathrm{m}^{-1}$, $A_{\mathrm{O_2}}^{\mathrm{spez}} = 10^4\ \ \mathrm{m}^{-1}$, and $A_{\mathrm{cryst}}^{\mathrm{spez},0} = 10^6\ \mathrm{m}^{-1}$; $A_{\mathrm{an}}^{\mathrm{spez}}$ is chosen to represent a non-porous lithium foil; the latter are $k_{\mathrm{an}}^{\mathrm{f}} = 3.84 \times 10^{15}\ \mathrm{mol\ m}^{-2}\ \mathrm{s}^{-1}$ ($\beta_{\mathrm{an}} = 0.5$) and $k_{\mathrm{ca}}^{\mathrm{f}} = 1.1 \times 10^{-17}\ \mathrm{m}^4\ \mathrm{mol}^{-3}\ \mathrm{s}^{-1}$ ($\beta_{\mathrm{ca}} = 0.09$).[77]

The surface energy γ of $LiOH \cdot H_2O$ is taken from the theoretical prediction of Mersmann[78]

$$\gamma = -0.414 \frac{kT}{a^2} \ln\left(c_{\mathrm{Li}^+}^{\mathrm{s}}\, V_{\mathrm{LiOH \cdot H_2O}}^{\mathrm{M}} \right) \tag{47}$$

which is in good agreement with the fits of Nielsen *et al.* to experiments.[59]

3.4 Simulation methodology

All simulations are performed with the multi-phase electrochemical simulation tool DENIS.[47,48] The computational domain is divided into 55 compartments with widths between 1 μm and 40 μm, simulations of flooded cathodes utilize a finer discretization at the oxygen inlet. The crystal size distribution is simulated with 29 discretization compartments. We use finite-volume discretization along the computational domain and upwind finite-element discretization for the crystal size distribution. Rate equations are evaluated using the software CANTERA.[79] The discretized equation system is numerically time-integrated with LIMEX.[80,81]

Table 2 Pitzer parameters for electrolyte volume, fitted to polynoms $g = \sum_n g_n \left(\frac{T}{K}\right)^n$

n	$V^0_{\mathrm{Li}^+}$	$M_{\mathrm{H_2O}}/V^0_{\mathrm{H_2O}}$ [83]	$\partial A^{\Phi}/\partial p$[84]	$\partial \beta_0^{\Phi}/\partial p$	$\partial \beta_1^{\Phi}/\partial p$	$\partial C^{\Phi}/\partial p$
-1	0	0	-2.437359×10^{-7}	0	0	0
0	7.314575×10^{-5}	-5.585541×10^{3}	3.776468×10^{-9}	$-7.217791 \times 10^{-10}$	-5.443222×10^{-9}	4.335196×10^{-10}
1	-7.532795×10^{-7}	9.323917×10^{1}	-2.333318×10^{-9}	2.833843×10^{-12}	4.358444×10^{-11}	$-1.404855 \times 10^{-12}$
2	2.524541×10^{-9}	-5.295044×10^{-1}	6.308666×10^{-14}	0	$-8.388285 \times 10^{-14}$	0
3	$-2.837367 \times 10^{-12}$	1.513766×10^{-3}	$-6.788572 \times 10^{-17}$	0	0	0
4	0	-2.181633×10^{-6}	0	0	0	0
5	0	1.261439×10^{-9}	0	0	0	0

4 Results and discussion

In this section we discuss the predictions of the model outlined in Sections 2 and 3. We concentrate on understanding and overcoming power and capacity limitations of aqueous Li–O_2 batteries. Above all, this paper highlights that in aqueous Li–O_2 batteries crystallization tends to occur close to the anode. Thus, we begin by explaining this inhomogeneous crystallization effect in Section 4.1. In Section 4.2 we demonstrate how GDEs offer higher power densities than flooded electrodes. By engineering the cell design, crystallization can be altered and cell capacities can be increased as described in Section 4.3.

4.1 Inhomogeneous precipitation

First, we study the galvanostatic discharge of a Li–O_2 battery with a GDE and a porous separator at moderately high currents $i = 10\ \mathrm{A\ m^{-2}}$ (see Fig. 7). Note that current densities are given with respect to the macroscopic separator area in this one-dimensional model. The cell takes 7.7 h to discharge. For comparison, commercial lithium-ion batteries can be completely discharged in less than 1 h at currents up to $i = 60\ \mathrm{A\ m^{-2}}$.[35,82]

The Li–O_2 battery discharges in two stages (see Fig. 7). Initially, up to point B, the salt concentration rises from its initial value to the solubility limit, the voltage decreases slowly, and $LiOH \cdot H_2O$ does not form. After point B, the salt concentration remains constant, slightly above its solubility limit, the voltage is constant, and the $LiOH \cdot H_2O$ volume fraction increases linearly in time. Eventually, at point D, an abrupt drop in cell voltage represents the end of discharge. This happens well before the mean volume fraction of $LiOH \cdot H_2O$ (*ca.* 0.095 at point D) reaches the void pore volume (0.375 for the electrode, 0.8 for the separator, *cf.* Table 1). During discharge, Li^+ forms at the anode and OH^- in the cathode. When the salt concentration increases, oxygen solubility decreases due to salting-out (see eqn (41)). Therefore, the cell voltage slightly decreases during this first stage. $LiOH \cdot H_2O$ crystals nucleate while the salt concentration is slightly overshooting at point B (this will be discussed below, *cf.* Fig. 11). Subsequently, $LiOH \cdot H_2O$ particles grow at a constant rate owing to a small but constant supersaturation and a constant precipitation surface area. During this period the cell voltage is nearly constant. This voltage plateau is typical for conversion reactions under stationary operating conditions, as for example observed in fuel cells. We explain the abrupt end of discharge in the following.

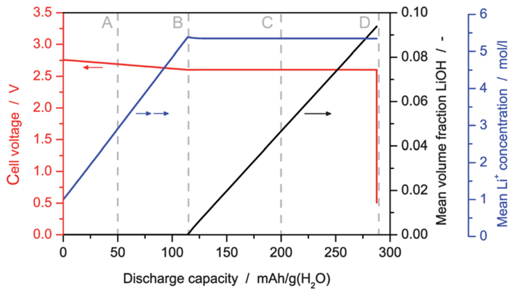

Fig. 7 Discharge of a Li–O_2 battery with a GDE and surface nucleation at $i = 10\ \mathrm{A\ m^{-2}}$. Cell voltage (red line), average volume fraction of $LiOH \cdot H_2O$ (black line), and average salt concentration (blue line) are shown. The dashed lines and capital letters refer to data shown in Fig. 8.

Fig. 8 shows spatial profiles of dissolved salt concentration, precipitate volume fraction, and the surface area of precipitation during discharge. At point A, we observe a salt concentration gradient with increasing concentration towards the separator and the anode. We emphasize that this is a fundamental property of aqueous Li–O_2 batteries due to the small transference number of Li^+ (see eqn (45)). Due to this small transference number, the electric potential in the electrolyte induces faster transport of OH^- than of Li^+. The salt concentration gradient must counteract this asymmetry in order to maintain electroneutrality. At point B, just after the nucleation phase, the specific surface area of precipitation shows that most crystal nuclei have formed next to the anode. Consequently, at point C, most $LiOH \cdot H_2O$ is present in this region. The concentration profile has regained a monotonous increase after the turmoil of nucleation, although inhomogeneous precipitation reduces its gradient. At point D, just before end of discharge, the reason for capacity limitation becomes obvious: A film of $LiOH \cdot H_2O$ forms at the separator/anode interface, completely blocking the lithium ion transport. The battery tries to overcome the transport limitations and further increases the salt concentration near the anode. This results in resumed nucleation (see also Fig. 11) and accelerated end of discharge.

In Fig. 9 we illustrate the role of convective flow for the cell performance. The pressure is approximately constant in the separator and drops from the separator towards the oxygen channel in the cathode. The magnitude of the pressure drop increases during cell discharge. It drives the convection of electrolyte from the separator into the GDE, where H_2O is constantly consumed in the oxygen reduction reaction (see eqn (5)). The

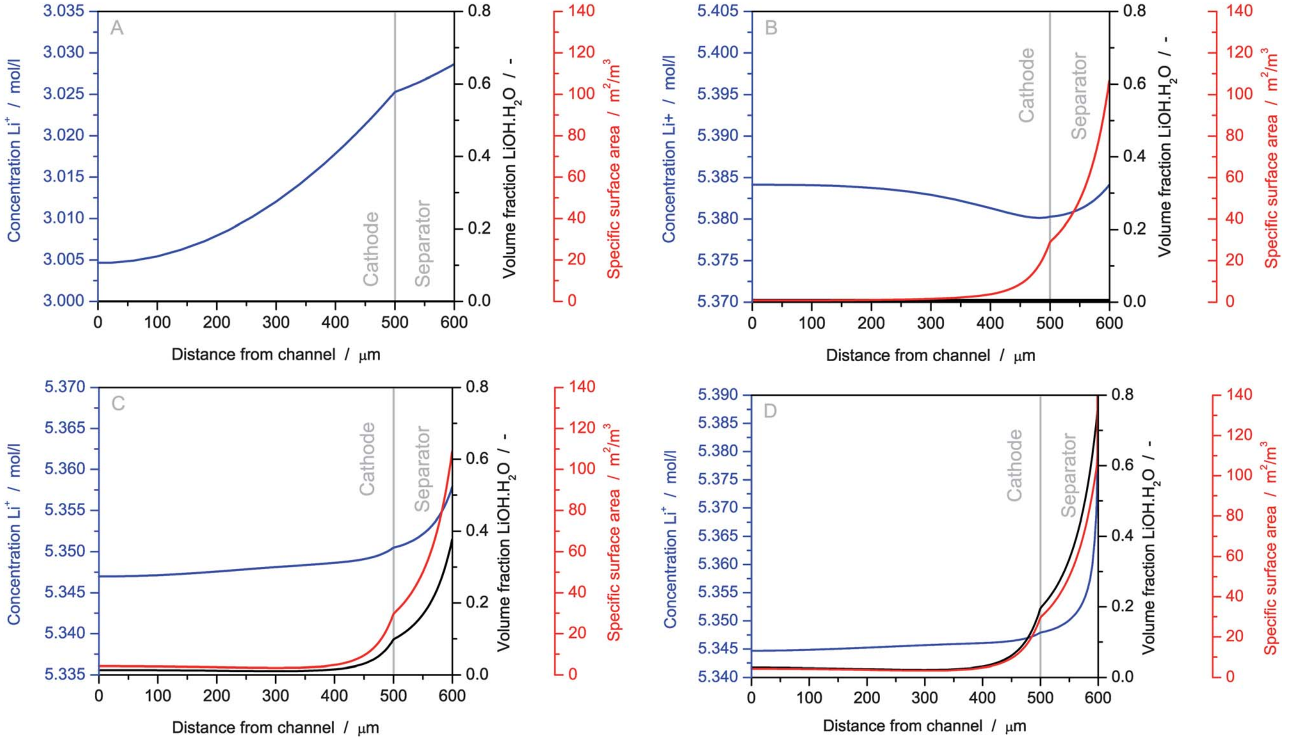

Fig. 8 Spatial profiles of salt concentration, volume fraction of $LiOH \cdot H_2O$ crystals, and the specific surface area of precipitation during galvanostatic cell discharge ($i = 10\ A\ m^{-2}$) at times A, B, C, D (see Fig. 7). Precipitation occurs mainly close to the anode due to the small transference number of Li^+ (see eqn (45)).

increasing drop reflects the increasingly inhomogeneous liquid phase saturation in the GDE (see eqn (18) and (36)) and leads to slightly inhomogeneous reaction rates in the GDE. The inset of Fig. 9 depicts the decrease in overall electrolyte pressure during cell discharge. The pressure decreases slowly and nonlinearly up to point B, it decreases fast and linearly after point B. The nonlinearity stems from the dependence of the liquid equation of state (see eqn (20)) on the salt concentration. After nucleation, the mean pressure decreases faster because H_2O is now consumed by $LiOH \cdot H_2O$ formation, too (see eqn (22)).

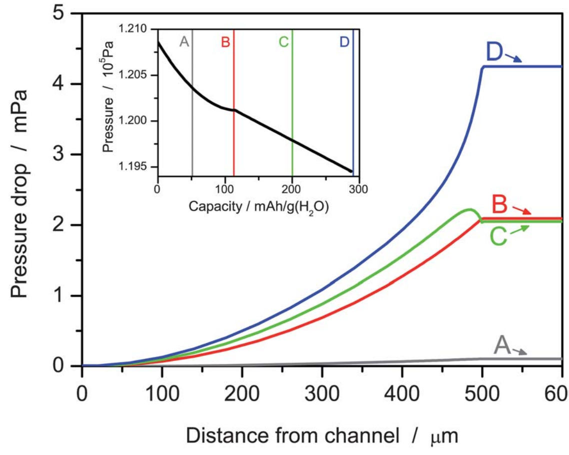

Fig. 9 Pressure drop in electrolyte during discharge of a $Li–O_2$ battery, normalized to $\Delta p = 0$ at the oxygen channel $y = 0$. The pressure drops inside the GDE from the separator to the oxygen channel, driving convective flow of electrolyte into the GDE. The inset depicts the average electrolyte pressure in the cell that decreases during discharge due to water consumption.

In summary, we have illustrated the main processes inside an aqueous $Li–O_2$ battery with a GDE during discharge. The cell fails due to inhomogeneous precipitation, particularly due to the formation of a film of $LiOH \cdot H_2O$ at the separator/anode interface. This prediction of our model agrees with experiments and explains the observed film of $LiOH \cdot H_2O$ on the anode-protecting membrane.[20]

4.2 Rate dependence

Fig. 10 shows the cell behavior during galvanostatic discharge at various currents. The discharge proceeds in the same way as described in Section 4.1 for all currents. An initial voltage drop due to polarization resistances (increasing with current) is followed by a slow linear voltage decrease due to salting-out. A constant voltage plateau occurs after the onset of $LiOH \cdot H_2O$ nucleation. The discharge ends abruptly due to inhomogeneous precipitation. The initial voltage drop is missing at low currents $i \leq 0.1\ A\ m^{-2}$ due to negligible overpotentials in the cathode. It is worth noting that the salt concentration reaches its solubility limit and $LiOH \cdot H_2O$ starts to nucleate at approximately the same capacity with respect to the mass of H_2O for any discharge rate; the amount of H_2O determines the amount of salt that can be dissolved in the cell. Most importantly, we observe that the discharge capacity is significantly rate-dependent for high currents $i \geq 10\ A\ m^{-2}$. At higher discharge currents the salt concentration gradient is larger and nucleation is more inhomogeneous. Therefore, precipitation is increasingly

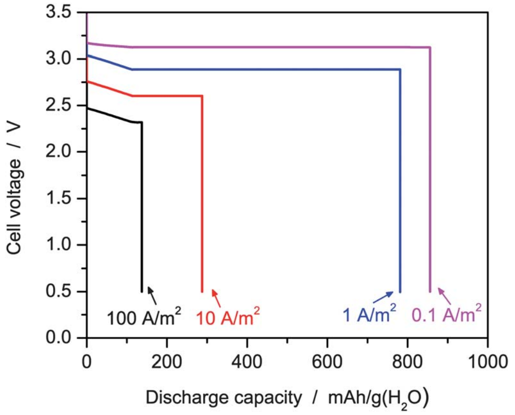

Fig. 10 Cell voltage during galvanostatic discharge of a Li–O$_2$ battery with a GDE for various discharge currents.

inhomogeneous and the capacity smaller with increasing discharge current.

The overvoltage at the voltage plateau increases with the logarithm of the discharge current in Fig. 10. This indicates that the discharge power is limited by the kinetics of the oxygen reduction reaction (see eqn (5)) in the cathode alone. The ionic transport is fast in aqueous electrolytes, indicated by the small concentration gradients shown in Fig. 8. Thus electrolyte transport and electrode tortuosity do not contribute significantly to the overvoltage at the discharge rates considered.

Analyzing the specific surface area for crystal growth illustrates the crystallization process (see Fig. 11). The surface area sharply increases twice, firstly, when precipitation begins (120 mA h $g_{H_2O}{}^{-1}$) and, secondly, when discharge ends. Between these events, the surface area is constant during discharge, yet, it depends significantly on current densities. The sharp rises of the surface area correspond to nucleation events. When the salt concentration reaches the critical supersaturation, crystal nucleation sets in. Supersaturation keeps increasing, until the nucleated particles support enough crystal growth. Then, supersaturation is reduced and nucleation stops. At larger discharge currents, more crystal nuclei are required to counteract dissolved salt formation. Therefore, the surface area for crystal growth increases with discharge current. At the end of discharge, transport of ions between the electrodes becomes restricted by precipitates. Consequently, the salt concentration must rise to overcome this and nucleation occurs again.

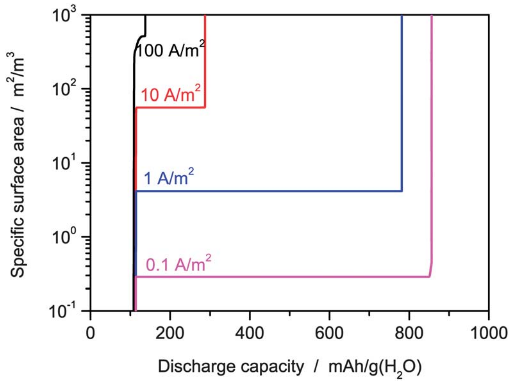

Fig. 11 Specific surface area for crystal growth in the separator region during cell discharge at various currents. After an initial nucleation period, the specific surface stays constant during crystal growth. At end of discharge, nucleation becomes dominant (see text).

In Fig. 12a and c we show the volume fraction of all phases at the end of discharge. Whereas the crystal volume fraction is very inhomogeneous at the moderately high current $i = 10$ A m^{-2} (see Fig. 12a), it is quite homogeneous at the small current $i = 0.1$ A m^{-2} (see Fig. 12). This is why inhomogeneous precipitation limits the discharge capacity at high rates only (see Fig. 10). We observe in Fig. 12c that free volume is still available in the GDE at the end of discharge. The water in the GDE has been consumed nearly completely and the electrolyte pressure cannot deliver additional water into the cathode. This means that inhomogeneous precipitation is not limiting the capacity at low rates.

For comparison, we investigate the discharge of a Li–O$_2$ battery with a flooded cathode. In this simulation, we neglect the liquid equation of state and electrolyte convection; the density of water is kept constant at $\rho_{H_2O} = 985$ kg m^{-3}; oxygen can only dissolve in the electrolyte from the gas channel. Therefore, oxygen transport is due to electrolyte diffusion only, which limits the cell performance. Resulting discharge behavior is shown in Fig. 13, and spatially resolved oxygen concentration profiles are shown in Fig. 14. Most importantly, battery power is strongly reduced in flooded electrodes, that is, voltages are ~500 mV lower. The flat voltage plateau observed for GDEs (Fig. 10) is absent for flooded cathodes, instead voltages are monotonically decreasing during discharge (Fig. 13). Large currents $i \geq 100$ A m^{-2} cannot even be sustained with flooded electrodes. As shown in Fig. 14, the reason for this behavior is the slow oxygen transport in the liquid phase of a flooded cathode, leading to large concentration gradients and confining electrochemical activity to an electrode volume close to the channel. The rate-dependent capacity (end of discharge) is again due to inhomogeneous precipitation, as discussed above for GDEs (see also Fig. 12b and d). In conclusion, GDEs offer significantly better performance because they strongly reduce oxygen transport limitations as compared to flooded electrodes.

4.3 Design of precipitation

After demonstrating the high performance of aqueous Li–O$_2$ batteries with GDEs, we further address the rate-dependent discharge capacity due to inhomogeneous precipitation. As pointed out earlier (see Section 2.5), aqueous electrolytes offer high conductivities and allow the use of large non-porous separator regions. In such separator regions, precipitation will probably occur on sedimenting dust particles (see Fig. 3b). In the GDE, however, crystals still nucleate on surfaces. The single unknown parameter in our nucleation model is the density of nucleation sites N_0 (see eqn (25)). One can imagine designing this number by voluntarily adding dust particles. This motivates our approach to optimize the discharge capacity by varying the number of nucleation sites.

We illustrate the effect of varying the number of nucleation sites in the separator region, N_0, with Fig. 15 by discussing the

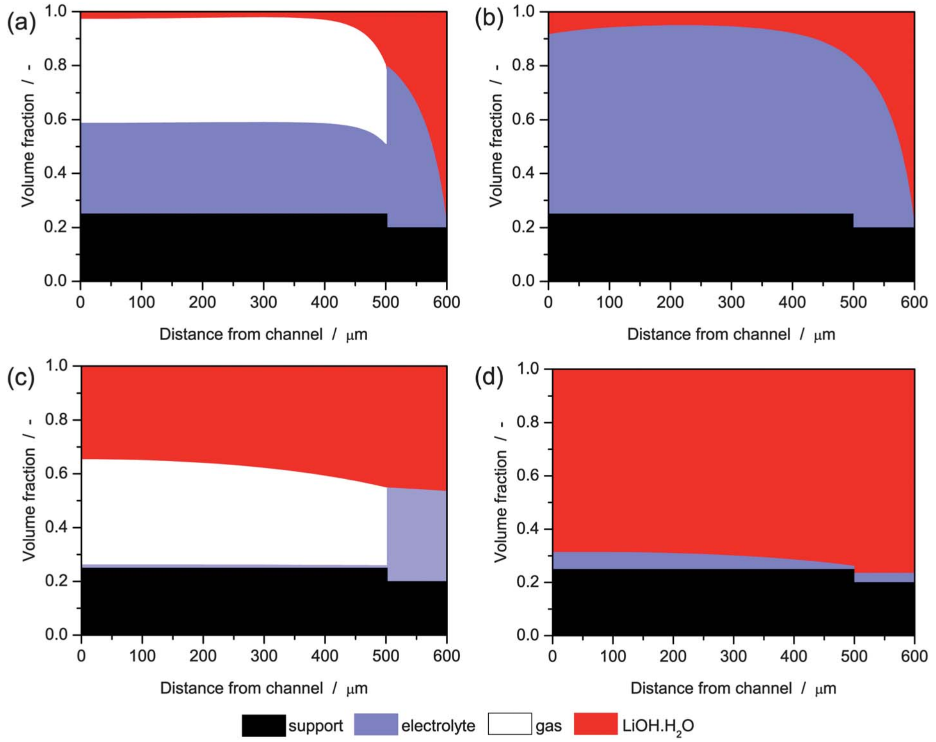

Fig. 12 Volume fraction of phases at end of galvanostatic discharge for a (a) GDE at $i = 10$ A m^{-2}, (b) flooded electrode at $i = 10$ A m^{-2}, (c) GDE at $i = 0.1$ A m^{-2}, and (d) flooded electrode at $i = 0.1$ A m^{-2}.

electrolyte volume at the end of discharge. For small N_0, more crystals nucleate in the cathode than in the separator and consequently discharge ends due to electrolyte depletion at the cathode–separator surface. For large N_0, instead, most crystals nucleate in the separator and discharge ends due to electrolyte depletion in the separator. At intermediate N_0, LiOH·H$_2$O grows uniformly in the cathode and the separator. Taking into account achievable water purities and surface defect densities, experimental values might be slightly higher than the optimum value $N_0 = 10^{18.5}$ m^{-3} found with this model. However, crystallization outside the cathode is advantageous because it avoids the problem of passivation of active surfaces.

This optimization of the cell capacity is summarized for different N_0 in Fig. 16. The cell capacity is maximum at intermediate N_0, when precipitation occurs in both cathode and separator regions. A bulk separator region has the advantage that external forces (*i.e.*, stirring) can be applied in order to homogenize the sedimented LiOH·H$_2$O, schematically described by eqn (35). This stirring process does not affect the cell performance at low N_0, when precipitation in the cathode dominates. But it is advantageous for large N_0, when precipitation in the separator is critical to cell performance.

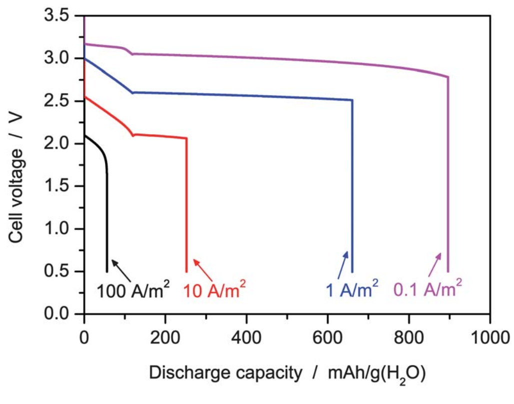

Fig. 13 Cell voltage during galvanostatic discharge of a Li–O$_2$ battery with a flooded electrode (see text) for various discharge currents.

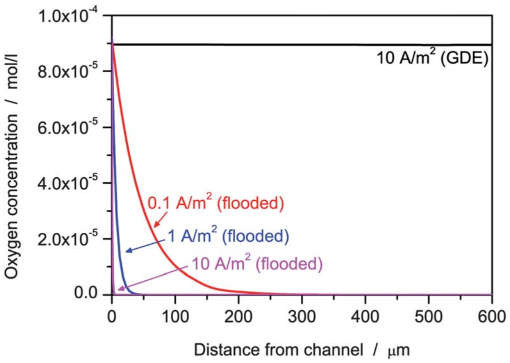

Fig. 14 Dissolved oxygen concentration profile along cell coordinates at 50% SOC for a GDE (see Fig. 7) and a flooded electrode (see Fig. 13). The concentration rapidly drops in the flooded electrode due to the low diffusivity of oxygen in water, even at moderate discharge currents. In the GDE the oxygen concentration is nearly constant.

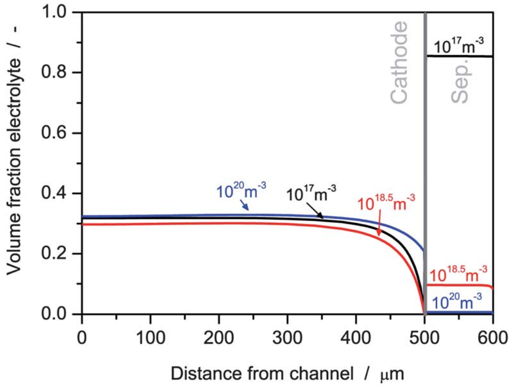

Fig. 15 Volume fraction of a electrolyte at end of discharge with nucleation on dust particles and stirring at various N_0 (see red dots in Fig. 16). At large N_0 precipitation occurs mainly in the cathode, at small N_0 precipitation mainly occurs in the separator. Cell capacity is largest at intermediate N_0 (see Fig. 16).

The surface energy γ is another important parameter for adjusting the classical theory of nucleation and growth to experiments.[59] In this paper we choose $\gamma = 0.026kT/a^2$ (see eqn (47)), justified by theory and experiments.[78] A sensitivity analysis of the discharge capacity on γ is presented in Fig. 17. By varying γ over one order of magnitude, we vary the nucleation barrier by two orders of magnitude (see eqn (24)). Without stirring the capacity increases significantly with γ. With stirring the capacity is higher and slightly depends on the surface energy non-monotonically. A greater surface energy generates a greater nucleation barrier and a greater critical supersaturation. Thus, the ratio of salt concentration gradient and critical supersaturation decreases with γ so that precipitation becomes more homogeneous. Without stirring this directly results in an increased capacity. Because stirring creates homogeneous deposits, it enables good capacities even at low critical supersaturations and low γ. The non-monotonic behaviour of the capacity with stirring is due to the complex interplay of inhomogeneous precipitation in cathode and separator regions with different void volumes and nucleation kinetics. To summarize, we find that our model results are sensitive to the exact value of the surface energy γ for precipitation of $LiOH \cdot H_2O$. However, our general conclusions remain valid and the optimized cell depends on γ only weakly.

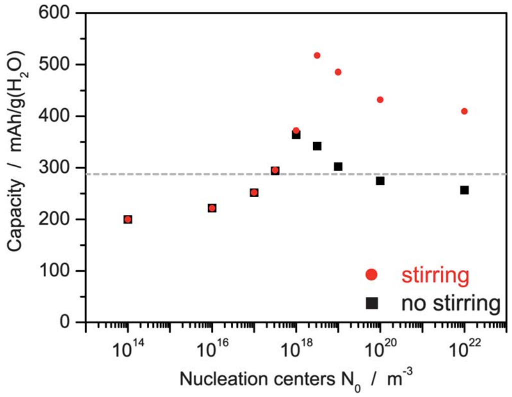

Fig. 16 Discharge capacity of a Li–O_2 battery after galvanostatic discharge at i = 10 A m^{-2} with nucleation on dust particles (see Section 2.6) as a function of density of nucleation centers in the separator N_0. The capacity for nucleation on surfaces from Fig. 7 is included as a gray line. The capacity increases at large N_0, when the $LiOH \cdot H_2O$ crystals are actively stirred (red dots) compared to the situation without stirring (black squares).

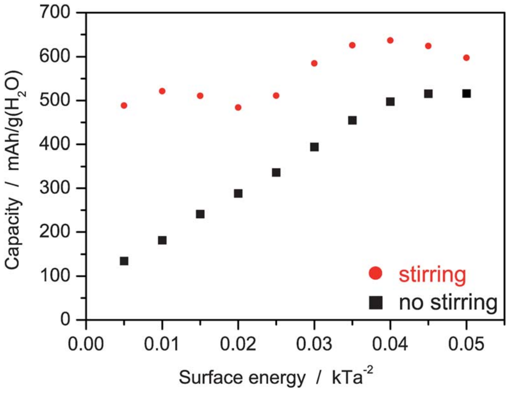

Fig. 17 Discharge capacity of a Li–O_2 battery after galvanostatic discharge at i = 10 A m^{-2} with nucleation on dust particles (see Section 2.6) as a function of surface energy γ, that is, the nucleation barrier (see eqn (24)). The number of nucleation centers $N_0 = 10^{18.5}$ is chosen to optimize the capacity (see Fig. 16). In this article we use the surface energy $\gamma = 0.026kT/a^2$ from theoretical predictions,[78] which agree with measurements.[59] Our simulation results strongly depend on the nucleation barrier.

During the discharge we keep track of the particle size of sedimenting nuclei. A typical distribution is shown in Fig. 18. The particle radius $r \sim 10, \ldots, 100$ µm is determined by the interplay of crystal growth and sedimentation. The size distribution depicted varies along the cell dimension due to inhomogeneous nucleation.

Finally, in Fig. 19 we compare the energy density of galvanostatic discharge of the three designs studied here: First, a GDE with a porous separator, second a flooded cathode with a porous separator, and third a GDE with a bulk separator. In the third case, we use optimized conditions, that is, nucleation on dust particles in the separator, stirring, and $N_0 = 10^{18.5}$ m^{-3}. We observe that flooded electrodes show energy densities comparable with GDEs at low discharge rates. However, they cannot deliver the current densities of modern lithium-ion batteries ($i \geq 10$ A m^{-2}). At high rates, corresponding to discharge in less than one hour ($i = 100$ A m^{-2}), GDEs offer three times larger cell capacities. If we adjust the cell design to the precipitation process, we can reduce capacity fading and further increase the energy density at high rates. A next optimization step would be to enlarge the separator region, which would reduce the relative mass overhead in the cell.

We close this section with a brief outlook on the influence of inhomogeneous precipitation and cell design concepts on charging. On the one hand, a deposit-free cathode offers undisturbed electrochemical surface reactions and transport paths also during charge. On the other hand, inhomogeneously distributed precipitates may limit power densities during charge. While the driving force for dissolution, that is, the difference between salt concentration and solubility, is greater within the porous cathode, the reaction area for dissolution is

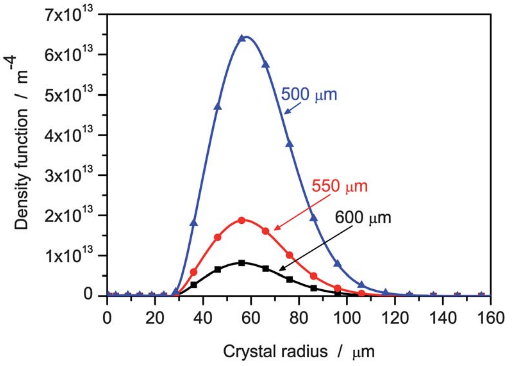

Fig. 18 Particle size distribution density (see eqn (29)) at $y = 600$ μm (blue), $y = 550$ μm (red), $y = 500$ μm (black) at 50% SOC during galvanostatic discharge of a Li–O_2 battery ($i = 10$ A m^{-2}) with nucleation on dust particles and stirring. The lines are interpolations of the simulation results (squares, dots, and triangles). The number of nucleation centers $N_0 = 10^{18.5}$ is chosen to optimize the capacity (see Fig. 16).

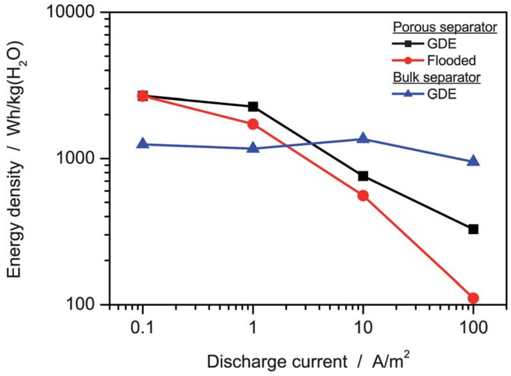

Fig. 19 Energy density of a Li–O_2 battery with different designs: a GDE with surface nucleation, a flooded electrode with surface nucleation, and a bulk separator with nucleation on sedimenting dust particles and stirring. In the latter case, the number of nucleation centers $N_0 = 10^{18.5}$ is chosen to optimize the capacity at $i = 10$ A m^{-2} (see Fig. 16).

greater in the porous separator close to the anode. In a realistic cycling scenario, these effects will not balance each other and cycling efficiency will be reduced. In a bulk separator, however, this issue can be solved by actively distributing the precipitate in the separator, for example by rotating the battery. This would increase the area for dissolution significantly. In summary, a bulk separator region is also advantageous during charging.

5 Conclusions

Lithium–oxygen (Li–O_2) batteries have recently received great attention due to their large theoretical specific energy. Advantages of the aqueous design include the stability of the electrolyte, the existing long-term experience with gas diffusion electrodes (GDEs), and the solubility of the reaction product lithium hydroxide. Not many experimental results on aqueous Li–O_2 batteries have been published, because a number of challenges must be overcome, including the need for a suitable lithium-ion-conducting membrane, a durable lithium metal anode, and strategies to mitigate carbon dioxide poisoning. In this situation, mathematical models have the unique potential to analyze and optimize the fundamental operating principle and therefore support cell development in its initial stages.

In this article we have presented the development and application of a multi-physics continuum model of aqueous Li–O_2 batteries with gas diffusion electrodes. A particular feature of the model is the detailed description of precipitation dynamics based on the classical theory of nucleation and growth. Parameters were taken from the extensive published literature on aqueous solutions. Therefore, the model is completely determined by measured parameters.

Simulations of discharge behavior, including detailed spatiotemporal analysis, were performed for different cell designs and operating conditions. The results showed that batteries with GDEs have high power densities and flat discharge curves. They are superior to cells with flooded electrodes. Inhomogeneous precipitation of solid $LiOH \cdot H_2O$ was predicted to be the capacity-limiting process at high discharge rates relevant for applications. At these rates, precipitation was shown to occur predominantly at the interface between the separator and the anode. This can be interpreted as formation of a solid product film on the anode, explaining earlier experimental findings.[20] Note that this tends to keep solid and insulating reaction products out of the porous cathode, possibly a huge advantage over non-aqueous Li–O_2 batteries. Further simulations showed that the capacity limitation can be reduced by adapting the cell design to the underlying physical processes. Therefore, precipitation of reaction products will not be a key problem for aqueous Li–O_2 batteries. Solid reaction products are in fact necessary to reach competitive energy densities.

To conclude, this paper highlights two major advantages of aqueous Li–O_2 batteries over non-aqueous designs. First, the availability of GDEs reduces limitations due to slow oxygen diffusion. Second, precipitation tends to occur outside of the cathode and to not poison the active surfaces in the cathode. These specific advantages tend to be neglected among the multitude of research on non-aqueous Li–O_2 batteries.

List of symbols

Symbol	Unit	Meaning
α_i	—	Symmetry factor
β	—	Bruggeman coefficient
δ, δ_0	m	Diffusion layer thickness around $LiOH \cdot H_2O$ nucleus
η_j	kg s^{-1} m^{-1}	Viscosity of phase
ε_j	m^3 m^{-3}	Volume fraction of phase
γ	J m^{-2}	Surface energy of $LiOH \cdot H_2O$
$\bar{\kappa}_k$	m^3 mol^{-1} Pa^{-1}	Partial molar compressibility of species
κ^D	A m^{-1}	Transport parameter of lithium hydroxide solution
κ	A V^{-1} m^{-1}	Conductivity of lithium hydroxide solution
μ_i	J mol^{-1}	Chemical potential of species
μ_i^0	J mol^{-1}	Chemical potential of species in the standard state
$\Delta\mu_i$	J mol^{-1}	Partial molar Gibbs reaction enthalpy

(Contd.)

Symbol	Unit	Meaning
Φ_j	V	Electric potential of phase
$\Delta\Phi_i$	V	Electric potential step for reaction
ρ_k	kg m^{-3}	Mass density of species
$A(n)$	m^2	Surface area of $LiOH \cdot H_2O$ nucleus
a	m	Length scale of $LiOH \cdot H_2O$, $a = (V_{\text{cryst}}^{\text{M}})^{1/3} {N_{\text{A}}}^{-1}$
a_{D}	m	Length scale of $LiOH^{\text{aq}}$, $a_{\text{D}} = (c_{\text{Li}^+})^{-1/3} {N_{\text{A}}}^{-1}$
a_k	—	Activity of species
A_k^{spez}	m^2 m^{-3}	Specific surface of reaction
B_j	m^2	Permeability of porous material
C	m^{-2} s^{-1}	Coefficient for stirring of $LiOH \cdot H_2O$ reservoir
c_k	mol m^{-3}	Concentration of species
c_k^{s}	mol m^{-3}	Solubility of species
D_0	m^2 s^{-1}	Self-diffusion coefficient of Li^+
D_k	m^2 s^{-1}	Diffusion coefficient of species
D_k^{M}	mol m^{-1} s^{-1} V^{-1}	Migration coefficient of species
E	W h kg^{-1}	Gravimetric energy density
$f(r)$, $N(r)$	m^{-1}, —	Size distribution of $LiOH \cdot H_2O$ nucleus
ΔG, ΔG_{crit}, ΔG_{V}, ΔG_{A}	J mol^{-1}	Formation energy of crystal nucleus
g	m s^{-2}	Standard gravity
h	M	Height of battery cell
H	mol m^{-3} Pa^{-1}	Henry's constant
H_k^0	J mol^{-1}	Standard partial molar enthalpy of species
h_k^{Θ}, s_k^{Θ}, $c_k^{\text{p},\Theta}$		Thermodynamic data of species
$\vec{j}_{\pm}^{\text{D}}$, $\vec{j}_{\pm}^{\text{M}}$	mol m^{-2} s^{-1}	Diffusion and migration flux
$J(s)$	Pa	Leverett function
k_i^{f}, k_i^{r}		Forward and backward kinetic coefficient of reaction
M_k	kg mol^{-1}	Molar mass of species
n, n_{crit}	—	Number of particles in $LiOH \cdot H_2O$ nucleus
N_0	m^{-3}	Number of nucleation sites
$\dot{N}$	s^{-1} m^{-3}	Nucleation rate of $LiOH \cdot H_2O$
N_j	mol	Number of particle of phase or species
p_k	Pa	Partial pressure of species, pressure of phase
r	m	Radius of $LiOH \cdot H_2O$ nucleus
S	—	Relative supersaturation of LiOH
S_k^0	J mol^{-1}	Standard partial molar entropy of species
$\dot{s}_i$	mol m^{-2} s^{-1}	Rate of reaction
s	—	Saturation of the liquid phase in GDE
t_k	—	Transference number of species
U_0	V	Open-circuit voltage
V_j^{M}	m^3 mol^{-1}	Molar volume of phase
ν^{g}	m s^{-1}	Velocity of sedimentation
$\bar{V}_k$	m^3 mol^{-1}	Partial molar volume of species
$\vec{v}_j$	m s^{-1}	Convection velocity of phase
V_j	m^3	Volume of phase
y	m	Coordinate along modelling domain
Z	—	Zeldovitch factor
z_k	—	Charge number of species

List of constants

Symbol	Value
F	96 485.256 A s mol^{-1}
k	1.380662×10^{-23} J K^{-1}
N_{A}	6.0221367×10^{23} mol^{-1}
p_0	101 325 Pa
R	8.3145353 J k^{-1} mol^{-1}
T_0	298.15 K

Notes and references

1 G. Girishkumar, B. McCloskey, A. C. Luntz, S. Swanson and W. Wilcke, *J. Phys. Chem. Lett.*, 2010, **1**, 2193.

2 J. Christensen, P. Albertus, R. S. Sanchez-Carrera, T. Lohmann, B. Kozinsky, R. Liedtke, J. Ahmed and A. Kojic, *J. Electrochem. Soc.*, 2012, **159**, R1.

3 P. G. Bruce, S. A. Freunberger, L. J. Hardwick and J.-M. Tarascon, *Nat. Mater.*, 2012, **11**, 19.

4 Y.-C. Lu, B. M. Gallant, D. G. Kwabi, J. R. Harding, R. R. Mitchell, M. S. Whittingham and Y. Shao-Horn, *Energy Environ. Sci.*, 2013, **6**, 750.

5 B. Scrosati, J. Hassoun and Y.-K. Sun, *Energy Environ. Sci.*, 2011, **4**, 3287.

6 C.-X. Zu and H. Li, *Energy Environ. Sci.*, 2011, **4**, 2614.

7 K. M. Abraham and Z. Jiang, *J. Electrochem. Soc.*, 1996, **143**, 1.

8 S. A. Freunberger, Y. Chen, Z. Peng, J. M. Griffin, L. J. Hardwick, F. Bardé, P. Novák and P. G. Bruce, *J. Am. Chem. Soc.*, 2011, **133**, 8040.

9 F. Mizuno, S. Nakanishi, Y. Kotani, S. Yokoishi and I. Hideki, *Electrochemistry*, 2010, **78**, 403.

10 R. Black, S. H. Oh, J.-H. Lee, T. Yim, B. Adams and L. F. Nazar, *J. Am. Chem. Soc.*, 2012, **134**, 2902.

11 B. D. McCloskey, R. Scheffler, A. Speidel, D. S. Bethune, R. M. Shelby and A. C. Luntz, *J. Am. Chem. Soc.*, 2011, **133**, 18038.

12 B. D. Mccloskey, A. Speidel, R. Scheffler, D. C. Miller, V. Viswanathan, J. S. Hummelshøj, J. K. Nørskov and A. C. Luntz, *J. Phys. Chem. Lett.*, 2012, **3**, 997.

13 Z. Peng, S. A. Freunberger, Y. Chen and P. G. Bruce, *Science*, 2012, **337**, 563.

14 G. Chase, S. Zecevic, W. Walker, J. Uddin, K. Sasaki, V. Giordani, V. Bryantsev, M. Blanco and D. Addison, International Patent application no. 2011033821, 2010.

15 B. Kumar, J. Kumar, R. Leese, J. P. Fellner, S. J. Rodrigues and K. M. Abraham, *J. Electrochem. Soc.*, 2010, **157**(1), A50.

16 H. Kitaura and H. Zhou, *Energy Environ. Sci.*, 2012, **5**, 9077.

17 F. Beck and P. Rüetschi, *Electrochim. Acta*, 2000, **45**, 2467.

18 K. Suto, S. Nakanishi, H. Iba and K. Nishio, An Aqueous Li–Air Battery Based on a Novel Reservoir Concept, in *15th International Meeting on Lithium Batteries*, Montreal, 2010.

19 J. Suntivich, H. A. Gasteiger, N. Yabuuchi, H. Nakanishi, J. B. Goodenough and Y. Shao-Horn, *Nat. Chem.*, 2011, **3**, 546.

20 P. Stevens, G. Toussaint, G. Caillon, P. Viaud, P. Vinatier, C. Cantau, O. Fichet, C. Sarrazin and M. Mallouki, *ECS Trans.*, 2010, **28**, 1.

21 Y. Wang and H. Zhou, *J. Power Sources*, 2010, **195**, 358.

22 H. He, W. Niu, N. M. Asl, J. Salim, R. Chen and Y. Kim, *Electrochim. Acta*, 2012, **67**, 87.

23 F. Bidault, D. J. L. Brett, P. H. Middleton and N. P. Brandon, *J. Power Sources*, 2009, **187**, 39.

24 D. Tromans, *Ind. Eng. Chem. Fundam.*, 2000, **39**, 805.

25 C. Monnin and M. Dubois, *J. Chem. Eng. Data*, 2005, **50**, 1109.

26 S. F. Bender, J. W. Cretzmeyer and T. F. Reise, in *Handbook of Batteries*, ed. D. Linden and T. B. Reddy, McGraw-Hill, New York, 2002.

27 T. Springer and T. Zawodzinski, *J. Electrochem. Soc.*, 1991, **138**, 2334.

28 J. P. Zheng, P. Andrei, M. Hendrickson and E. J. Plichta, *J. Electrochem. Soc.*, 2011, **158**, A43.

29 J. S. Newman and K. E. Thomas-Alyea, *Electrochemical Systems*, J. Wiley, 2004.

30 M. Doyle, T. F. Fuller and J. Newman, *J. Electrochem. Soc.*, 1993, **140**, 1526.

31 V. Ramadesigan, P. W. C. Northrop, S. De, S. Santhanagopalan, R. D. Braatz and V. R. Subramanian, *J. Electrochem. Soc.*, 2012, **159**, R31.

32 T. R. Ferguson and M. Z. Bazant, *J. Electrochem. Soc.*, 2012, **159**, A1967.

33 W. Dreyer, J. Jamnik, C. Guhlke, R. Huth, J. Moskon and M. Gaberscek, *Nat. Mater.*, 2010, **9**, 448.

34 W. Dreyer, C. Guhlke and R. Huth, *Phys. D*, 2011, **240**, 1008.

35 C. Hellwig, S. Sörgel and W. G. Bessler, *ECS Trans.*, 2011, **32**, 215.

36 W. Lai and F. Ciucci, *Electrochim. Acta*, 2011, **56**, 4369.

37 W. Lai and F. Ciucci, *Electrochim. Acta*, 2010, **56**, 531.

38 M. Z. Bazant, 2012, arXiv:1208.1587.

39 P. Bai, D. A. Cogswell and M. Z. Bazant, *Nano Lett.*, 2011, **11**, 4890.

40 R. Malik, F. Zhou and G. Ceder, *Nat. Mater.*, 2011, **10**, 587.

41 D. A. Cogswell and M. Z. Bazant, *ACS Nano*, 2012, **6**, 2215.

42 S. S. Sandhu, J. P. Fellner and G. W. Brutchen, *J. Power Sources*, 2007, **164**, 365.

43 R. E. Williford and J.-G. Zhang, *J. Power Sources*, 2009, **194**, 1164.

44 P. Andrei, J. P. Zheng, M. Hendrickson and E. J. Plichta, *J. Electrochem. Soc.*, 2010, **157**, A1287.

45 P. Albertus, G. Girishkumar, B. McCloskey, R. S. Sánchez-Carrera, B. Kozinsky, J. Christensen and A. C. Luntz, *J. Electrochem. Soc.*, 2011, **158**, A343.

46 Y. Wang, *Electrochim. Acta*, 2012, **75**, 239.

47 J. P. Neidhardt, D. N. Fronczek, T. Jahnke, T. Danner, B. Horstmann and W. G. Bessler, *J. Electrochem. Soc.*, 2012, **159**, A1528.

48 W. Bessler, S. Gewies and M. Vogler, *Electrochim. Acta*, 2007, **53**, 1782.

49 I. W. Eames, N. J. Marr and H. Sabir, *Int. J. Heat Mass Transfer*, 1997, **40**, 2963.

50 A. Latz and J. Zausch, *J. Power Sources*, 2011, **196**, 3296.

51 D. M. Bernardi and M. W. Verbrugge, *J. Electrochem. Soc.*, 1992, **139**, 2477.

52 E. C. Kumbur, K. V. Sharp and M. M. Mench, *J. Electrochem. Soc.*, 2007, **154**, B1315.

53 E. C. Kumbur, K. V. Sharp and M. M. Mench, *J. Electrochem. Soc.*, 2007, **154**, B1305.

54 E. C. Kumbur, K. V. Sharp and M. M. Mench, *J. Electrochem. Soc.*, 2007, **154**, B1295.

55 J. Nyvlt, O. Söhnel, M. Matuchova and M. Broul, *The Kinetics of Industrial Crystallization*, ed. J. Skrivanek, ACADEMIA, Prague, 1985, p. 350.

56 O. Söhnel and J. Garside, *Precipitation: Basic Principles and Industrial Applications*, Butterworth-Heinemann, Oxford, 1992, p. 391.

57 J. W. Mullin, *Crystallization*, Butterworth-Heinemann, Oxford, 4th edn, 2001, p. 594.

58 D. Kashchiev and G. M. van Rosmalen, *Cryst. Res. Technol.*, 2003, **38**, 555.

59 A. E. Nielsen and O. Sohnel, *J. Cryst. Growth*, 1971, **11**, 233.

60 A. E. Nielsen, *J. Cryst. Growth*, 1984, **67**, 289.

61 R. N. Singh and A. C. Chatterji, *J. Phys. Chem.*, 1958, **62**, 1408.

62 S. G. Rinaldo, W. Lee, J. Stumper and M. Eikerling, *Electrochem. Solid-State Lett.*, 2011, **14**, B47.

63 P. W. Atkins and J. De Paula, *Atkins' Physical Chemistry*, Oxford University Press, Oxford, 2006.

64 D. Tromans, *Hydrometallurgy*, 1998, **48**, 327.

65 W. Lang and R. Zander, *Ind. Eng. Chem. Fundam.*, 1986, **25**, 775.

66 A. J. Elliot, M. P. Chenier and D. C. Ouellette, *Fusion Eng. Des.*, 1990, **13**, 29.

67 K. S. Pitzer, in *Activity Coefficients in Electrolyte Solutions*, ed. K. S. Pitzer, CRC Press Inc., Boca Raton, FL, 1991.

68 N. M. Moller, *Geochim. Cosmochim. Acta*, 1988, **52**, 821.

69 T. M. Herrington, A. D. Pethybrldge and M. Roffey, *J. Chem. Eng. Data*, 1986, **31**, 31.

70 A. H. Roux, G. Perron and J. E. Desnoyers, *Can. J. Chem.*, 1984, **62**, 878.

71 F. J. Millero, G. K. Ward and P. V. Chetirkin, *J. Acoust. Soc. Am.*, 1977, **61**, 1492.

72 M. Laliberte, *J. Chem. Eng. Data*, 2007, **52**, 321.

73 E. L. Littauer and K. C. Tsai, *Electrochim. Acta*, 1979, **24**, 351.

74 P. Han and D. M. Bartels, *J. Phys. Chem.*, 1996, **100**, 5597.

75 P. J. Gierszewski, R. C. Prasad and D. W. Kirk, *Fusion Eng. Des.*, 1992, **15**, 279.

76 N. Zamel, X. Li, J. Becker and A. Wiegmann, *Int. J. Hydrogen Energy*, 2011, **36**, 5466.

77 S. Pinnow, N. Chavan and T. Turek, *J. Appl. Electrochem.*, 2011, **41**, 1053.

78 A. Mersmann, *J. Cryst. Growth*, 1990, **102**, 841.

79 D. G. Goodwin, Cantera, http://code.google.com/p/cantera.

80 R. Ehrig, U. Nowak, L. Oeverdieck and P. Deuflhard, in *High performance scientific and engineering computing. Lecture notes in computational science and engineering*, ed. H.-J. Bungartz, F. Durst and C. Zenger, Springer, 1999, p. 233.

81 P. Deuflhard, E. Hairer and J. Zugck, *Numer. Math.*, 1987, **51**, 501.

82 M. Safari and C. Delacourt, *J. Electrochem. Soc.*, 2011, **158**, A562.

83 *CRC Handbook of Chemistry and Physics*, ed. D. R. Lide, CRC Press Inc., Boca Raton, FL, 89th edn, 2008.

84 J. Ananthaswamy and G. Atkinson, *J. Chem. Eng. Data*, 1984, **29**, 81.